ADVANCED INTELLIGENT SYSTEMS
www.advintellsyst.com

Super-Resolution Photothermal Imaging at the Microscale by Model-Based Image Reconstruction

Luca Presotto, Mario Marini, Giuseppe Chirico, Laura Sironi, Laura D'Alfonso, Davide Panzeri, Amirbahador Zeynali, Reha Akpinar, Luca Di Tommaso, Margaux Bouzin, and Maddalena Collini*

Super-resolution strategies expand the applicability of imaging modalities toward previously inaccessible spatial scales. Herein, photoactivated far-infrared thermography is pushed from the millimeter to the micrometer scale by a 2D super-resolution imaging approach capable of tackling the resolution barriers imposed by both diffraction-limited signal collection and lateral spatiotemporal heat diffusion. The proposed imaging strategy relies on a full-wave forward model of far-infrared thermography and on an image-inversion approach, which reconstructs the surface distribution of the sample photothermal absorbers via gradient-descent optimization as the one yielding the best match between predicted and experimental images. With minute-long acquisitions on a commercial low-cost far-infrared camera, less-than-5 μm spatial resolution is demonstrated on both synthetic samples and human liver biopsies ex vivo, thereby exemplifying the applicability of super-resolution photothermal imaging to the fast nondestructive characterization of biological specimens well below the tissue spatial scale.

1. Introduction

Infrared noncontact thermal imaging provides thermographic sequences based on the intensity of the thermal radiation emitted by the sample and detected by a mid-/far-infrared (IR) thermal camera.[1] According to Stefan–Boltzmann's law under the assumption of gray-body emission, the fourth-power temperature dependence of the sample radiance allows a conceptually straightforward quantification of the sample temperature with high sensitivity and no sample invasiveness.[1,2]

Temperature sensitivities have been pushed down to the 20–40 mK range,[3,4] and the temporal resolution of state-of-the-art IR thermography setups, which is typically assigned by the 30–100 Hz imaging rate of microbolometer-based far-IR cameras,[3] can be pushed to a faster ≈kHz acquisition rate with more expensive cooled mid-IR devices.[5] More severe limitations affect the imaging spatial resolution instead. As predicted by the pioneering work of Abbe,[6] diffraction nominally limits the achievable resolution to the tens-to-hundreds μm range depending on the detected IR signal wavelength and on the numerical aperture of the camera collecting lens. However, differently from the case of optical (fluorescence) microscopy, where diffraction and Abbe's law completely determine the theoretical resolution limit of the imaging system,[7] the radial spatial resolution of thermography is severely impacted by the diffusive nature of heat conduction across the sample surface:[8] at fixed thermal diffusivity/conductivity, the lateral diffusive propagation of thermal waves turns the spatial resolution into an increasing function of time, to the point where the nominal diffraction-limited 300 μm spatial resolution of our commercial low-cost far-IR camera can easily broaden to an effective >1 mm resolution with an imaging time as low as few seconds.[9] Such a degrading property of heat conduction is particularly detrimental for the application of IR thermography to both defect/inhomogeneity/delamination detection in nondestructive material testing[10,11] and the characterization of soft-matter samples below the tissue scale.

Along with techniques aimed at improving the signal-to-noise ratio of thermographic images[11] (e.g., lock-in thermography and thermal pulse compression), various software and hardware super-resolution (SR) approaches have been developed. Software-based SR image processing enhances the resolution of digital imaging sensors by subpixel image localization and pixel reassignment techniques and has been implemented in commercial IR camera systems already.[12,13] By the exploitation of nonredundant low-resolution frames acquired under relative geometric displacements, it typically allows a fourfold resolution gain.[13,14] A similar upsampling factor of 4–8 can be obtained by machine learning-based methods, which apply SR concepts to solve

L. Presotto, M. Marini, G. Chirico, L. Sironi, L. D'Alfonso, D. Panzeri, A. Zeynali, M. Bouzin, M. Collini
Physics Department
Università degli Studi di Milano-Bicocca
Piazza della Scienza 3, 20126 Milano, Italy
E-mail: margaux.bouzin@unimib.it

R. Akpinar, L. Di Tommaso
Biomedical Sciences Department
Humanitas University
Via R. Levi Montalcini 4, 20072 Pieve Emanuele, Italy

The ORCID identification number(s) for the author(s) of this article can be found under https://doi.org/10.1002/aisy.202300510.

DOI: 10.1002/aisy.202300510

computer-vision tasks such as object detection, recognition, and segmentation in IR images.[13,15,16] Techniques relying on deep convolutional neural network (CNN) pipelines, borrowed from visible-spectrum imaging[17] and trained on aligned low- and high-resolution image pairs or triplets,[15,16,18] have been advantageously applied to passive thermography.[19] As typical for CNNs, however, one needs large-size training and test datasets acquired on similar samples, making the trained models specific to a particular scenario and limiting their generalizability.[18,19] Furthermore, software-based SR methods improve the effective sampling frequency without changing the detector size,[14] but do not necessarily aim at super-resolving the image content below the thermally diffused diffraction-limited camera point spread function (PSF). They are mainly intended for imaging at the macroscale and find application in surveillance/security, automation, and industrial performance monitoring.

Resolution enhancements at the mesoscale have been attempted by hardware-based active methods, where a controlled thermal gradient is forced inside the sample by means of focused excitation laser sources.[8,11,20] The combination of structured heating via pseudorandom blind laser illumination patterns and numerical methods of compressed sensing (e.g., iterative joint sparsity algorithms) has been applied to thermographic data[8,11,20] with a fourfold lateral resolution enhancement over the thermal PSF[5,8,10] deep inside the imaged sample. Along with the so-called virtual-wave approach,[11] structured heating and compressed sensing optimization have been mainly applied to the 3D reconstruction of subsurface material defects: defects have been reconstructed in depth on the 0.5–1 mm spatial scale[11,12,21] and up to defect distance-to-depth ratios of 1:4, provided that target heterogeneities were sufficiently rare for the application of sparsity-based regularizations.

Active SR thermal imaging at the sample surface can be performed on a sub-mm scale by coupling structured illumination in the form of modulated laser raster scanning with the a posteriori localization of the resulting isolated laser-induced temperature increments.[9] As recently demonstrated on biological tissues[22,23] and historical cultural heritage artifacts[24] by our group, the spatial resolution can be pushed down to the tens of μm range with a nearly 20-time resolution enhancement relatively to the thermally diffused PSF of the adopted camera in conventional operation.[9] Such high achievable resolution is enhanced, however, at the expense of the duration of image reconstruction. The necessity of localizing sequentially induced individual temperature increments translates into hour-long data acquisition times over mm^2- to cm^2-sized sample areas.[9]

In this framework, we tackle here the development and experimental validation of an SR active thermal imaging approach capable of faster (minute-long) quantitative surface temperature mapping at <5 μm lateral spatial resolution on a low-cost (≈5 k€) commercial thermal camera operating in the far-IR. We relax the constraints on the detection of isolated temperature variations and implement structured heating by the simple continuous raster scan of focused visible laser light. Given the resulting distribution of spatially and/or temporally overlapping laser-induced temperature variations, we exploit the full-wave forward modeling of heat diffusion according to the 3D heat equation and cast the reconstruction of the underlying 2D distribution of the photothermal absorbers at the sample surface in the form of an offline model-based image inversion. By means of the solution of the inverse problem, iteratively performed via gradient-descent optimization, we achieve the subdiffraction localization of the sample light-absorbing entities and the quantitative measurement of the laser-induced temperature profile.

We provide here at first full validation of the proposed approach by proof-of-principle experiments on synthetic samples. We prove accurate image reconstruction within minute-long data acquisition and demonstrate that the imaging resolution and contrast largely outperform those enabled by existing state-of-the-art SR IR imaging techniques. We test the robustness of our model-based image-inversion algorithm against variations in the sample thermal properties and excitation laser scan parameters, and experimentally demonstrate a >200-fold gain over the mm-sized thermal PSF of the employed camera in conventional acquisition mode on the seconds timescale. Biophysical application of microscale photothermal imaging is finally exemplified on ex vivo human liver biopsy specimens, where the detected temperature increments allow mapping the spatial distribution of Perls' Prussian blue (PB)-stained hepatic iron depositions associated to hereditary hemochromatosis (HH). By pushing fast and quantitative thermal imaging down to the microscale, our results pave the way to the application of IR thermography to the active thermal characterization of complex materials in all branches of the applied physical and life sciences, from cultural heritage conservation to biomedical technology.

2. Results

2.1. Forward Model of IR Thermography and Image Reconstruction Algorithm

Structured illumination is at the basis of our SR imaging strategy. We prime light absorption and the photothermal effect by scanning a low-power focused laser beam along a conventional raster path and detect the resulting distribution of temperature increments by a far-IR thermal camera in a temporal image sequence. Information on the underlying spatial distribution of (endogenous or exogenous) sample photothermal absorbers, which is encoded and unresolved in the raw thermal camera frames, is extracted a posteriori by an image-inversion approach based on gradient-descent optimization. Similar to what has been proposed for SR nondestructive defect detection,[21] the spatiotemporal temperature profile detected by the camera is iteratively compared with the theoretical prediction obtained by integrating the 3D heat equation. Our theoretical model fully accounts for signal diffraction at the collection optics and for pixelated camera-based detection, and the distribution of the photothermal entities at the sample surface is identified as the one yielding the best match between computed and experimental images. In summary, the principle of model-based thermal image reconstruction consists in accounting for both thermal diffusion effects and diffraction-limited signal detection in a full-wave forward model of active thermography, and in computationally addressing the corresponding inverse problem to identify the target distribution of heat-releasing entities well

below the resolution limits imposed by the thermal camera in conventional operation.

Formally, image reconstruction can be formulated as the identification of an a priori unknown high-resolution temperature distribution ΔT_{SR} from the experimentally observed low-resolution temperature distribution $\Delta T_{\mathrm{LR}}^{\mathrm{exp}}$ according to a theoretical functional form

$$\Delta T_{\mathrm{LR}}^{\mathrm{exp}} = f(\Delta T_{\mathrm{SR}}) \tag{1}$$

Dimensionally, for a raster scan path along a $N_x \times N_y$ pixel grid, ΔT_{SR} is a $N_x \times N_y$ matrix. Its pixel size coincides with the scan pixel size on the sample plane, hereafter referred to as Δx. $\Delta T_{\mathrm{LR}}^{\mathrm{exp}}$ is a 3D matrix instead, consisting of N_{frames} images acquired by the camera at fixed frame rate f_{rate} during the laser scan. As the scan pixel size (≈1–10 μm) is chosen to be much smaller than the camera pixel size on the sample plane (≈400 μm), the scanned area is entirely contained within a small region of interest (ROI) in the acquired raw thermal camera frames. The analysis is limited therefore to a ROI encompassing $N_x^{\mathrm{TC}} \times N_y^{\mathrm{TC}}$ pixels, and $\Delta T_{\mathrm{LR}}^{\mathrm{exp}}$ consists overall of $N_x^{\mathrm{TC}} \times N_y^{\mathrm{TC}} \times N_{\mathrm{frames}}$ values. The operator f in Equation (1) allows reconstructing ΔT_{SR} by modeling, in order, 1) the deposition of energy on the sample plane by the excitation laser spot, 2) the diffusion of the heat released by the sample in space and time, 3) the imaging process via the optics PSF, and 4) the low-resolution signal sampling on the pixelated sensor of the camera. All these steps are, or can be successfully approximated by, linear operators.

We start from theoretically describing the temperature increment predicted by the solution of the 3D heat equation for a homogeneous opaque solid slab, having thickness L, isotropic thermal diffusivity D, and thermal conductivity k, which is immersed in air at room temperature T_0 and subject to low-power continuous-wave visible laser illumination.[25] The sample temperature $T(\mathbf{r}, t)$ ($\mathbf{r} = (x, y, z)$) satisfies

$$\frac{k}{D}\frac{\partial T(\mathbf{r},t)}{\partial t} - k\nabla^2 T(\mathbf{r}, t) = Q(\mathbf{r}, t) \tag{2}$$

with boundary conditions

$$\begin{cases} -k\left.\dfrac{\partial T(\mathbf{r},t)}{\partial z}\right|_{z=0} = -h[T(x,y,0,t) - T_0] - \varepsilon\sigma\left[T^4(x,y,0,t) - T_0^4\right] \\ -k\left.\dfrac{\partial T(\mathbf{r},t)}{\partial z}\right|_{z=L} = h[T(x,y,L,t) - T_0] + \varepsilon\sigma\left[T^4(x,y,L,t) - T_0^4\right] \end{cases} \tag{3}$$

Convective losses are modeled in Equation (3) by a constant coefficient of surface heat transfer h, whereas radiative losses are modeled according to Stefan–Boltzmann's law under the assumption of gray-body emission with emissivity ε. The source term Q in Equation (2) describes the Gaussian laser beam, with intensity I_0 and $1/e^2$ radius ω, that impinges on the sample front surface $z = 0$ in a conventional raster scan with pixel dwell time τ_{on} and scan pixel size Δx. For surface absorption by an opaque sample, its explicit analytical expression can be cast in the form

$$\begin{aligned} Q(x,y,0,t) &= I_0 \cdot a(x,y) \cdot g(x,y,t) \equiv \\ &\equiv I_0 \cdot a(x,y) \cdot \exp\left[-2\frac{(x-\overline{x})^2 + (y-\overline{y})^2}{\omega^2}\right] \\ &\quad * \sum_{m=1}^{N_x}\sum_{n=1}^{N_y} \delta(\overline{x} - m\Delta x, \overline{y} - n\Delta x)\Pi_{t_{m,n}, t_{m,n}+\tau_{\mathrm{on}}}(t) \end{aligned} \tag{4}$$

$a(x,y) \in [0,1]$ is the space-dependent absorption coefficient at the excitation wavelength on the sample surface, whereas $g(x,y,t)$ provides the Gaussian beam amplitude and spatiotemporal distribution in the xy-plane, respectively. In this notation, $\overline{x}$ and $\overline{y}$ represent the center (peak) coordinates of the excitation laser beam. As $\overline{x}$ and $\overline{y}$ should vary as a function of time to describe the laser displacement along the raster scan grid, a dependence on $\overline{x}$ and $\overline{y}$ is included in the double sum over the indexes m and n: for each pair of sum indexes (i.e., for each pixel (m, n) on the scan grid), the spatial Dirac delta makes the $\overline{x}$ and $\overline{y}$ coordinates in the Gaussian laser beam shape assume the desired values $\overline{x} = m\Delta x$ and $\overline{y} = n\Delta x$. Temporally, if the scan starts at pixel $(0, 0)$ at time point $t = 0$, the laser hits pixel (m, n) of the scan grid at time point $t_{m,n} = ((n-1)N_x + m - 1)\tau_{\mathrm{on}}$. This is accounted for by the boxcar function $\Pi_{t_{m,n}, t_{m,n}+\tau_{\mathrm{on}}}(t)$, defined with unit amplitude in the interval $(t_{m,n}, t_{m,n} + \tau_{\mathrm{on}})$ and zero amplitude elsewhere.

Even though no exact close-form analytical solution can be retrieved for Equation (2)–(4), approximate solutions can be derived under the assumptions of thermally thick or thermally thin sample with negligible radiation and convection losses.[25] The approximations simplify the theoretical treatment but guarantee wide applicability, covering any sample thickness of practical relevance.[24] In the case of thermally thin sample (Biot's number $hL/k \ll 1$) and of infinitely thick sample ($L \to +\infty$),[25] respectively, the local surface temperature $T(x, y, z = 0, t)$ solving Equation (2)–(4) can be derived[25] as

$$\begin{aligned} T(x,y,t) &= T_0 + \Delta T(x,y,t) \cong T_0 \\ &\quad + \sum_{m=1}^{N_x}\sum_{n=1}^{N_y} \frac{I_0 a(x,y) D}{kL} \int_{t_0}^{t} \frac{\omega^2}{\omega^2 + 8Dt_1} \\ &\quad \times \exp\left(-\frac{2((x-m\Delta x)^2 + (y-n\Delta x)^2)}{\omega^2 + 8Dt_1}\right)\exp\left(-\frac{2Dht_1}{kL}\right)dt_1 \end{aligned} \tag{5a}$$

and

$$\begin{aligned} T(x,y,t) &= T_0 + \Delta T(x,y,t) \cong T_0 \\ &\quad + \sum_{m=1}^{N_x}\sum_{n=1}^{N_y} \frac{I_0 a(x,y) D}{k} \int_{t_0}^{t} \frac{\omega^2}{\omega^2 + 8Dt_1} \\ &\quad \times \exp\left(-\frac{2((x-m\Delta x)^2 + (y-n\Delta x)^2)}{\omega^2 + 8Dt_1}\right)\frac{1}{\sqrt{\pi D t_1}}dt_1 \end{aligned} \tag{5b}$$

The lower integration limit t_0 contains a dependence on the sum indexes m and n: provided that pixel (m, n) is illuminated at time $t_{m,n}$, the lower integration limit is $t_0 = t_{m,n}$ if $t < t_{m,n} + \tau_{\mathrm{on}}$, whereas $t_0 = t + t_{m,n} - \tau_{\mathrm{on}}$ if $t \geq t_{m,n} + \tau_{\mathrm{on}}$.

Bearing in mind that we aim at detecting laser-primed temperature increments by an IR thermal camera, the continuous

temperature profile $T(x, y, 0, t)$ predicted on the sample plane has to be spatially convoluted with the Gaussian-shaped camera point spread function and discretized over square pixels of side ℓ equal to the camera pixel size[24] (Figure S1, Supporting Information). At time t, the (i, j)-th pixel in the thermal camera images senses, therefore, a PSF-convoluted and pixel-averaged temperature increment $\Delta T_{\mathrm{LR}}(i, j, t)$ $(i = 1 \ldots N_x^{\mathrm{TC}}, j = 1 \ldots N_y^{\mathrm{TC}})$, which can be explicitly computed as

$$\begin{aligned}\Delta T_{\mathrm{LR}}(i,j,t) &= \sqrt[4]{[(T_0 + \Delta T(x,y,t))^4 * \mathrm{PSF}(x,y)] * \Pi^{2\mathrm{D}}_{i,j,\ell}(x,y)} \\ &- \sqrt[4]{T_0^4} \approx \sqrt[4]{\left[\left(T_0^4 + 4T_0^3\Delta T\right) * \mathrm{PSF}\right] * \Pi^{2\mathrm{D}}_{i,j,\ell}} \\ &- T_0 = \sqrt[4]{T_0^4 + 4T_0^3\Delta T * \mathrm{PSF} * \Pi^{2\mathrm{D}}_{i,j,\ell}} \\ &- T_0 = \sqrt[4]{T_0^4\left(1 + \tfrac{4}{T_0}\Delta T * \mathrm{PSF} * \Pi^{2\mathrm{D}}_{i,j,\ell}\right)} \\ &- T_0 \approx T_0\left(1 + \tfrac{1}{T_0}\Delta T * \mathrm{PSF} * \Pi^{2\mathrm{D}}_{i,j,\ell}\right) - T_0 \\ &= \Delta T * \mathrm{PSF} * \Pi^{2\mathrm{D}}_{i,j,\ell}\end{aligned} \tag{6}$$

$\Pi^{2\mathrm{D}}_{i,j,\ell}(x, y)$ denotes here the operation of spatial averaging over pixel (i, j) of the thermal camera; spatial averaging and the convolution with the PSF do not impact the baseline temperature T_0, which is constant in space. Equation (6) accounts for the quartic temperature dependence of the number of collected IR photons as predicted by Stefan–Boltzmann's law, and applies the Mc Laurin expansion $(1 + \Delta T)^\alpha \approx 1 + \alpha\Delta T$: with a typical $T_0 \approx 293\mathrm{K}$ and $\Delta T \approx 10\mathrm{K}$, the approximation $(T_0 + \Delta T)^4 \approx T_0^4 + 4T_0^3\Delta T$ holds within a 5% underestimate of the exact value.[9]

The result of Equation (6) should be finally discretized in time to account for the fixed camera frame rate: $\Delta T_{\mathrm{LR}}(i, j, t)$ is averaged over time intervals having length equal to $1/f_{\mathrm{rate}}$ by a temporal convolution with a 1D boxcar function $\Pi^{1\mathrm{D}}_{k,\mathrm{f}_{\mathrm{rate}}}(t)$ $(k = 1 \ldots N_{\mathrm{frames}})$:

$$\Delta T_{\mathrm{LR}}(i,j,k) = \Delta T_{\mathrm{LR}}(i,j,t) * \Pi^{1\mathrm{D}}_{k,\mathrm{f}_{\mathrm{rate}}}(t) \tag{7}$$

If we now assume a uniform light absorption coefficient $a(m, n)$ within each scan pixel, $\Delta T_{\mathrm{LR}}(i, j, k)$ can be expressed as the sum of spatial convolutions, each term being linearly dependent on $a(m, n)$ itself:

$$\begin{aligned}\Delta T_{\mathrm{LR}}(i,j,k) &= \Delta T(x,y,0,t) * \mathrm{PSF} * \Pi^{2\mathrm{D}}_{i,j,\ell} * \Pi^{1\mathrm{D}}_{k,\mathrm{f}_{\mathrm{rate}}} \\ &= \sum_{m=1}^{N_x}\sum_{n=1}^{N_y} a(m,n)\left[\mathscr{F}(x,y,t;m,n) * \mathrm{PSF} * \Pi^{2\mathrm{D}}_{i,j,\ell} * \Pi^{1\mathrm{D}}_{k,\mathrm{f}_{\mathrm{rate}}}\right]\end{aligned} \tag{8}$$

The function $\mathscr{F}$, which is defined based on the expression for $\Delta T(x, y, 0, t)$ in Equation (5a,b), is introduced here for the sake of compactness.

Overall, Equation (5)–(8) formulate the necessary full-wave forward model of IR thermography and allow computing the expected thermal camera image sequence for any absorption map and given set of laser scan parameters and sample thermal properties. The best estimate of the unknown absorption map a can now be accessed by minimizing the discrepancy between the theoretical prediction $\Delta T_{\mathrm{LR}}(i, j, k)$ and the experimentally measured temperature increments $\Delta T^{\mathrm{exp}}_{\mathrm{LR}}(i, j, k)$. The reconstruction of all the elements $a(m, n)$ of the matrix a can be cast, therefore, in the form of an unconstrained least-squares minimization problem according to

$$a = \underset{a}{\operatorname{argmin}}\left\{\sum_k\sum_i\sum_j\left[\Delta T_{\mathrm{LR}}(i,j,k) - \Delta T^{\mathrm{exp}}_{\mathrm{LR}}(i,j,k)\right]^2\right\} \tag{9}$$

Sums run over all pixels of the thermal camera ROI and over all the time points in the acquired image sequence.

As the forward model is not analytically invertible for $a(m, n)$, the implementation of Equation (9) is performed via gradient-descent optimization as detailed in Section S1, Supporting Information. Once the best estimate of the absorption coefficient matrix has been retrieved, the same full-wave forward model is finally exploited to convert it into a SR $N_x \times N_y$ image of temperature increments $\Delta T_{\mathrm{SR}}(m, n)$. Each ΔT_{SR} value provides the temperature increment that the thermal camera would quantify in the presence of a single isolated laser pulse centered on pixel (m, n) and lasting τ_{on}.

A summarizing schematic flow chart of the proposed iterative reconstruction algorithm is depicted in **Figure 1**.

2.2. Experimental Section/Methods

2.2.1. IR Thermography

A custom-made benchtop optical setup has been employed for the SR thermography experiments of Figure 2–4. The excitation source is a continuous-wave He–Ne laser beam ($\lambda_{\mathrm{exc}} = 633$ nm, power $P = 1.5$ mW on the sample plane; Thorlabs Inc., NJ, USA). The scanning unit consists in a two-lens scan system (4 and 10 cm focal lengths) followed by either a 10 cm lens or a 20×0.4-N.A. air objective (Carton, JP) for beam focalization. A beam expanding unit allows adjusting the excitation laser beam waist, with the tightest exploited $1/e^2$ beam radius ω on the sample plane equaling 7.5 and 0.9 μm with the 10 cm lens and the 20× objective, respectively. The scanning unit is coupled

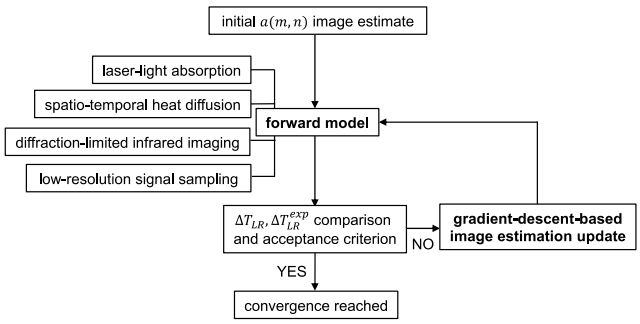

Figure 1. Schematic diagram of SR model-based thermal image reconstruction. An initial guess for the absorption coefficient image $a(m, n)$ is fed to the full-wave forward model of IR thermography to predict a low-resolution image ΔT_{LR} of the laser-induced temperature variations on the sample. $a(m, n)$ is iteratively updated until convergence is reached by gradient-descent optimization to minimize the discrepancy between the computed ΔT_{LR} image and the experimentally measured values $\Delta T^{\mathrm{exp}}_{\mathrm{LR}}$.

to two galvanometric mirrors (MicroMax Series 670, Cambridge Technology Inc., MA, USA) driven by a programmable board (LabVIEW RIO, National Instruments, TX, USA), which operates the mirrors in raster scanning mode on a $N_x \times N_y$ grid with adjustable pixel size Δx on the sample plane and pixel dwell time τ_{on}. The total imaging time is $t_{\text{tot}} = N_x \times N_y \times \tau_{\text{on}}$; data acquisition might be repeated twice to account for image acquisition getting paused during a few second-long calibrations automatically performed by the thermal camera.

Signal detection is performed in reflection configuration by collecting the IR photon emission of the laser-excited sample front surface. For optically transparent samples, transmission mode is exploited when the 20× microscope objective is in use due to geometrical constraints imposed by the objective working distance. In both cases, the employed uncooled microbolometer-based thermal camera (FLIR T650sc or FLIR E40, FLIR Systems Inc., OR, USA; 7.5–13 μm detection band, $f_{\text{rate}} = 30$ Hz) detects the thermal radiation with numerical aperture N.A. = 0.023 and pixel size $\ell \approx 400$ μm on the sample plane at the minimum camera-to-sample distance. Based on Abbe's diffraction law, the theoretical limit to the camera resolution is $\approx 0.6\,\lambda/\text{N.A.} = 0.26$ mm at the central 10 μm wavelength of the spectral detection band. Before each experiment, the pixel size ℓ is calibrated by imaging a known-size object at constant temperature to take small variations associated to the thermal camera positioning into account. Imaging of a stepper motor, which gets activated by a trigger signal at the very beginning of the laser scan, allows syncing the scan itself with the thermal camera acquisition.

For Figure 2e,g only, modulated laser raster scanning has been implemented on the same experimental setup as in ref. [9]: by means of a programmable shutter (Oriel 76992, Newport, CA, USA), synchronized with the scan, a laser deactivation time τ_{off} is introduced after each laser pulse lasting τ_{on} to guarantee the complete thermal relaxation of the sample in between consecutive excitation events. The resulting laser-induced temperature increments, separated in space and time, get subsequently localized by the nonlinear Gaussian surface fit of the thermal camera frames to assemble a SR image of the sample,[9] to be compared with the results of the model-based image reconstruction algorithm proposed in the present work.

For SR imaging on biological samples (Figure 5), a custom inverted two-photon excitation microscope (Nikon TE300, Nikon, JP) has been exploited as described elsewhere.[26] The excitation source is a Ti:Sa femtosecond laser (power $P = 10$ mW on the sample plane; Spectra Physics, CA, USA), employed here at $\lambda_{\text{exc}} = 800$ nm in continuous-wave mode. The beam is focused on the sample by a 20 × 0.5-N.A. air objective (PlanF, Zeiss, D) with $1/e^2$ beam radius $\omega = 1$ μm on the sample plane. At fixed laser beam, the sample is moved along an $N_x \times N_y$ raster path by means of a 3-axis piezo-driven stage (Hera P733 for xy scan, coupled to a Pifoc-P725 for z adjustment; Physik Instrument, D) with pixel size Δx on the sample plane and pixel dwell time τ_{on}. Signal detection has been performed with the FLIR E40 camera.

2.2.2. Optical Microscopy

Transmitted-light images of microfiche-printed samples have been acquired on a TCS SP5 STED-CW confocal microscope (Leica Microsystems, D). A 20 × 0.5-N.A. air objective (HCX PL Fluotar, Leica Microsystems, D) focuses a 633 nm He–Ne beam with ≈10 μW power on the sample plane, and transmitted light is collected by a nonspectral photomultiplier tube with no confocal pinhole. Images have been acquired in tile-scan mode with 400 Hz scan frequency per line.

Reference images of Perls' stained liver sections have been acquired by a Leica Thunder 3D Imager Tissue (Leica Microsystems, D). The system is implemented onto a DM6B-Z motorized microscope stand equipped with a Leica 40 × 0.8-N.A. HC PL FLUOTAR dry objective and a Leica DMC2900 RGB camera. A white light-emitting diode is collimated through Kohler illumination to achieve brightfield illumination. Before acquisition, white balancing is performed with the compensation utility included in the LAS X software suite (version 3.7.4.; Leica Microsystems, D). Whole-slide images (WSIs) have been collected by tile-scanning the sample with a 10% overlap between tiles. Each patch has been illuminated for 150 ms and imaged at the full resolution of the RGB camera (3.1 MP, 2048 × 1536 pixels). WSIs have a pixel size of 0.15 μm.

2.2.3. Materials

SR photothermal imaging has been tested on synthetic ink patterns produced on polyester (polyethylene terephthalate) substrates by microfiche printing. The photothermal ink layer, ≈1 μm in thickness on top of a polyester sheet with thickness $L = (180 \pm 30)$ μm, provides surface absorption with absorption coefficient $a = 0.6$ at the 633 nm excitation wavelength.[24] A sample emissivity $\varepsilon = (0.80 \pm 0.03)$ has been input to the thermal camera software as previously measured,[9] and the known polyester thermal conductivity $k = 0.2\ \text{Wm}^{-1}\,\text{K}^{-1}$ and thermal diffusivity $D = 3.4 \times 10^{-7}\ \text{m}^2\text{s}^{-1}$ have been assumed[24] for image reconstruction according to Equation (5a).

For the quantification of modulation transfer functions (MTFs) in Figure 4, matte black tape with known emissivity $\varepsilon = 0.96$, overlaid to a thermally thin 170 μm glass slide, has been exploited. The excitation beam has been focused on the tape at the sample rear surface and the IR thermal emission has been collected in transmission configuration. Heat diffusion is dominated by the glass substrate with thermal conductivity $k = 0.9\ \text{Wm}^{-1}\,\text{K}^{-1}$ and diffusivity $D = 5.0 \times 10^{-7}\ \text{m}^2\text{s}^{-1}$.

Human liver needle biopsies have been finally imaged in Figure 5. Slides have been prepared from formalin-fixed, paraffin-embedded tissues of hemosiderosis cases, with tissue sections 4 μm in thickness on top of a 1 mm thick glass slide. Sections have been stained with modified (no nuclear counterstain) Perl's PB by an automated stainer (Ventana BenchMark, Ventana Medical Systems, AZ, USA). All automated steps except from contra-staining (nuclear fast red) have been performed. For photothermal imaging, slides have been imaged in transmission geometry without mount and lamel cover. A sample emissivity $\varepsilon = 0.95$ has been adopted for stained biopsies, and Equation (5b) has been employed to describe the sample as thermally thick. Samples have been collected upon the patients' written consent and no further approval from the institutional ethics committee was required prior to the research on the archived sample.

2.2.4. Data Acquisition and Image Reconstruction Software

Photothermal imaging raw data have been acquired with the thermal camera software (FLIR Tools+, FLIR Systems Inc., OR, USA), exported in.csv file format, and entirely processed for model-based SR reconstruction by a custom written Python code. The code implements the full-wave forward model of IR thermography according to Equation (1)–(9) and gradient-descent optimization according to Section S1, Supporting Information. The offline image reconstruction lasts ≈5 min on a laptop computer with Apple M2 processor for the exemplary dataset of Figure 2c.

We neglect convective heat losses in Equation (5a,b). All imaging experiments have been performed indeed at 300 K room temperature and 1 atm pressure: with the heat transfer coefficient $h = 10\ \mathrm{Wm^{-2}\,K^{-1}}$ that is provided by the literature[24,27] for these imaging conditions (i.e., convection with air at standard temperature and pressure), heat losses do not practically impact measured temperature variations, as verified previously by our group by means of finite-element numerical simulations.[22] Additionally, the minimization of Equation (9) is carried out in principle over all the $N_x^{\mathrm{TC}} \times N_y^{\mathrm{TC}}$ pixels and time points of the acquired thermal camera image sequence: due to heat diffusion, the heat released in a given pixel upon a laser-light absorption event may propagate to all other pixels at later time points. In practical terms, due to the 0.1 K temperature sensitivity of the thermal camera and to the thermal diffusivity of the imaged sample, the heat released in each pixel is assumed to only contribute to the detected signal up to a maximum distance of 5 camera pixels (≈2 mm on the sample plane). The heat generated by laser light absorption at each pixel of the scan path is also assumed to contribute to the very same pixel for a maximum typical ≈10 s time interval by the implementation of a high-pass filter with ≈0.1 Hz frequency. This allows reducing the computational time during image reconstruction.

For the quantification of temperature increments, the baseline (room) temperature is quantified at each time point as the average temperature detected in a ROI lying outside the sample scanned area within the raw thermal camera frames.

The number of iterations for gradient-descent optimization typically lies in the range 10–50. For all datasets presented here, <10 iterations allow reconstructing the overall sample morphology already, with no substantial modification to the rendered image being achieved in subsequent iterations.

2.3. Proof-of-Principle Experiments

Model-based SR image reconstruction has been tested on synthetic reference samples produced by microfiche printing (Methods section). Such custom black ink patterns exhibit photothermal properties at the 633 nm excitation wavelength and can be designed at will to provide controlled subresolved structures with desired shape and characteristic dimensions in the ≈10–100 μm range. The same samples have been exploited previously by our group for the experimental validation of localization-based SR imaging[9] as well as for the experimental demonstration of novel quantitative thermal conductivity mapping protocols.[24]

An ink pattern mimicking the acronym LABS (Laboratory of Advanced Bio-Spectroscopy) (**Figure 2**a) has been imaged at first.

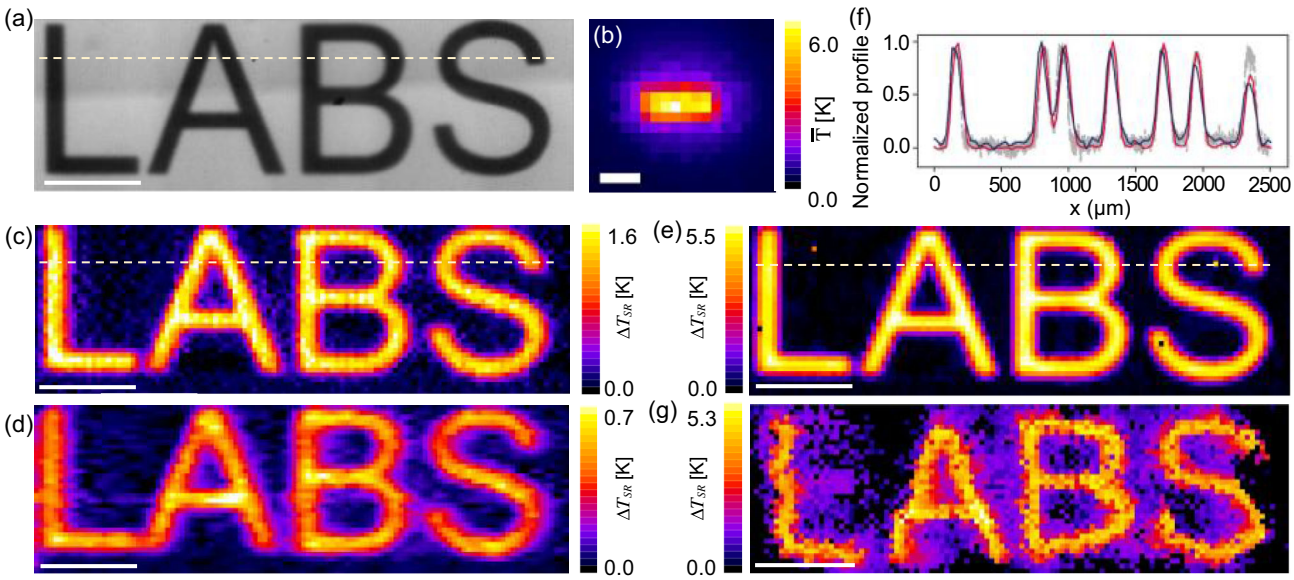

Figure 2. Proof-of-principle model-based SR image reconstruction. a) 633 nm transmitted-light image of a microfiche-printed sample. b) Temporal maximum projection of the raw thermal camera image sequence employed for the reconstruction of the image in (c). c,d) SR thermal images of the sample in (a) reconstructed by Equation (9) and acquired by laser raster scanning with parameters $N_x \times N_y = 120 \times 36$ and $\Delta x = 22.2\mu\mathrm{m}$; $\tau_{\mathrm{on}} = 50\mathrm{ms}$ in (c), $\tau_{\mathrm{on}} = 20\mathrm{ms}$ in (d). e,g) SR thermal images of the sample in (a) acquired by modulated laser raster scanning with parameters $N_x \times N_y = 120 \times 36$, $\Delta x = 22.2\mu\mathrm{m}$, $\tau_{\mathrm{on}} = 300\mathrm{ms}$, $\tau_{\mathrm{off}} = 0.9\mathrm{s}$; image reconstruction has been performed via Equation (9) for panel (e) and by the Gaussian fit and localization of individual laser-induced temperature increments according to ref. [9] for panel (g). f) Normalized intensity and temperature profiles extracted from the dashed yellow lines in panels (a,c,e) (grey, blue, and red, respectively). Laser beam waist $\omega = 28\mu\mathrm{m}$ everywhere; scale bars: 500 μm in (a,c–g), 2 mm in (b). All datasets have been acquired with the camera FLIR T650sc.

The excitation beam, focused to a 28 μm waist, has been raster scanned across the sample with 50 ms dwell time τ_{on} and 22 μm pixel size Δx. The acquired raw thermal camera image sequence has been fed to the full-wave forward model of IR thermography and gradient-descent optimization for image reconstruction according to Equation (9). The resulting SR image (Figure 2c) and its comparison with the optical transmitted-light image of the same sample employed here as high-resolution ground-truth frame (Figure 2a) demonstrate that the distribution of the sample endogenous photothermal entities is correctly recovered and that details as close as 100 μm are properly resolved: a very good match is indeed achieved between the experimental temperature profile and the theoretical prediction formulated according to the adopted forward model (Figure S2, Supporting Information). No detail of the reconstructed ink pattern is discernible instead in the corresponding raw conventional low-resolution thermal image of the same sample (Figure 2b).

In the acquisition of the dataset exploited for Figure 2c, multiple temperature increments induced by laser raster scanning necessarily get detected within the same thermal camera pixel because the scan pixel size $\Delta x = 22$ μm largely oversamples the 400 μm thermal camera pixel. With a typical thermal diffusivity $D \approx 10^{-7}\,\mathrm{m^2 s^{-1}}$, the heat generated by laser light absorption rapidly diffuses to the nearby scan pixel within a time of the order of $\Delta x^2/D \approx 5ms$. However, as the laser beam is displaced from one scan pixel to the next, the detected temperature temporal behavior alternates a sequence of thermal excitation and partial thermal relaxation phases. Consecutively induced temperature increments can be separated and identified by taking advantage of the information encoded in the temperature–time trace collected in each thermal camera pixel: we expect therefore that, at fixed thermal camera frame rate and scan pixel size, the resolution and contrast of the reconstructed image vary according to the laser scan speed (i.e., the dwell time τ_{on} at fixed field of view).

As predicted, at 30 Hz thermal camera frame rate, the SR image quality slightly worsens with a reduction of the laser pixel dwell time from 50 ms (Figure 2c) to 20 ms (Figure 2d), while it conversely improves when a laser deactivation time is introduced in between consecutive laser illumination events (Figure 2e). Still, we stress that that total imaging times of 3.6 and 1.4 min, respectively, achieved with the 50 and 20 ms dwell times, allow the reconstruction of SR images where the overall morphology of the photothermal ink pattern is perfectly discerned. Modulated laser raster scanning, implemented for Figure 2e, increases the imaging time to as much as 85 min over the same $2.8 \times 0.8\,\mathrm{mm^2}$ field of view while only moderately impacting image resolution and contrast (Figure 2f). Overall, Figure 2c–f provides a proof-of-principle demonstration of model-based IR image reconstruction at 100 μm resolution and validates the advantages of conventional raster scanning over modulated laser illumination.

The same dataset acquired by modulated laser raster scanning for Figure 2e can also be exploited for a quantitative comparison of model-based SR active thermography with the alternative state-of-the-art SR imaging approach previously proposed by our group.[9] Modulated raster scanning (implemented as described in the Methods section) primes indeed a sequence of spatially and temporally isolated temperature increments, which can be localized a posteriori by the automated surface Gaussian fit of raw thermal camera frames. A SR image can be reconstructed by the superposition of all the localized temperature variations, with their amplitude assigning the false-color code of the reconstructed image and with a spatial resolution that is only assigned by the signal-to-noise ratio of the acquired thermal camera frames and by the excitation laser beam waist.[9] The result, reported in Figure 2g, and its comparison with Figure 2e reveal that, on the very same dataset, model-based reconstruction leads to a SR image with better contrast and resolution. Figure 2c outperforms Figure 2g too, thereby confirming that, additionally to a dramatic 24-fold reduction in the total data acquisition time, the combination of a full-wave forward model of IR thermography with gradient-descent image inversion significantly improves the resolution and contrast of the reconstructed image relatively to previously developed SR strategies. Information on the amplitude of laser-primed temperature variations is also preserved, temperature variations quantified in Figure 2g being compatible with the corresponding values retrieved in Figure 2e according to Equation (5)–(9).

In the reconstruction of all the SR images reported in Figure 2c–e, the initial guess provided to the image inversion algorithm for the distribution of the sample absorption coefficient has consisted in a uniformly zero map $a(m,n) = 0$, i.e., initial uniformly zero temperature increments are compared to the raw thermal camera image sequence. Such an initialization—the least informative possible—does not require any prior assumption on the sample light-absorption properties while allowing successful reconstruction of the correct ink pattern. As investigated in Figure S3, Supporting Information, even assuming that prior knowledge could be incorporated in the initial image guess (e.g., by using Figure 2e as initialization for the reconstruction of the dataset exploited for Figure 2c), the SR image quality does not remarkably improve with respect to what is obtained with a uniformly zero initialization. Alternative guesses for the initial temperature-based image sequence, consisting in constant nonzero values or in randomly extracted values from a Gaussian distribution, lead to artifacts and an overall worse performance in image reconstruction (Figure S3, Supporting Information). Based on Figure S3, Supporting Information, initialization to $a(m,n) = 0$ has been therefore adopted throughout the present work.

2.3.1. Dependence on the Sample Thermal Properties and Scan Path

The proposed image reconstruction algorithm decodes the spatial distribution of the sample photothermal absorbers: it provides the absorption coefficient matrix $a(m,n)$ and converts it into an SR map $\Delta T_{SR}(m,n)$ of the temperature increments that would be detected by the thermal camera in the presence of single laser pulses lasting τ_{on}. To this aim, the sample thermal properties and a few instrumental parameters are required as input for the theoretical model of Equation (5)–(9). The thermal camera PSF, the camera pixel size on the sample plane, and the excitation laser beam waist are easily accessible by separate measurements. Different from ref. [11], we do not exploit blind

illumination, i.e., we assume we have exact knowledge of the laser illumination position at any time point. This approach reduces the problem complexity and does not affect the reconstruction robustness provided the laser positional noise can be neglected on the adopted experimental setup. The sample thermal diffusivity might be harder to access instead. We have tested therefore the robustness of the image reconstruction algorithm against variations in the assumed diffusivity value with **Figure 3**a and S4, Supporting Information. The dataset that has been analyzed with the known polyester diffusivity value $D = 3.35 \times 10^{-7}$ m^2s^{-1} for Figure 2c has been analyzed by systematically under- and overestimating the assumed diffusivity parameter in the reconstruction algorithm. The broad range $[0.41–26.8] \times 10^{-7}$ m^2s^{-1} has been explored, corresponding to the interval from one-eighth to eight times the exact polyester diffusivity value D. For each reconstructed image, the mean signal and background have been, respectively, quantified as the average detected temperature increments ΔT_{SR}^{max} and ΔT_{SR}^{min} in two ink-printed and plain polyester ROIs (Figure S4, Supporting Information). The image contrast, computed as $C = \left(\Delta T_{SR}^{max} - \Delta T_{SR}^{min}\right)/\left(\Delta T_{SR}^{max} + \Delta T_{SR}^{min}\right)$ and reported in Figure 3a as a function of the assumed diffusivity value, reveals the expected maximum value for $D = 3.35 \times 10^{-7}\ m^2\ s^{-1}$ and a maximum 35% decrease when the error in the diffusivity value is as high as 8 times. Still, it is worth remarking that the reconstructed ink pattern appears clearly readable across the entire spanned range of thermal diffusivity (Figure S4, Supporting Information), and that an 8-time error in the assumed diffusivity is much larger than the typical experimental uncertainty on the diffusivity itself (e.g., a factor of ten separates the diffusivities of polyester and stainless steel). The overall result of the analysis reported in Figure 3a and S4, Supporting Information, is that we can advantageously relax the request to a priori know the sample thermal properties when performing image reconstruction. At the same time, the bell shape of the data trend in Figure 3a suggests potential sensitivity in the measurement of the thermal diffusivity.

At fixed sample thermal diffusivity/conductivity and for a given distribution of the sample photothermal entities, we finally expect the direction of the laser scan path to possibly impact image reconstruction. Intuitively, a scan path that maximizes the space–time separation in between consecutive laser absorption events potentially simplifies image inversion. We have therefore imaged 60 µm ink stripes regularly spaced at 60 µm relative distance and maximized the polarization of the ink pattern relatively to the scan path by raster scanning parallel (Figure 3c) and orthogonally (Figure 3d) to the ink stripes. The comparison with the ground-truth optical transmitted-light image of the sample (Figure 3b,e) demonstrates that parallel scanning improves the image visibility, but the 60 µm ink stripes are resolved irrespective of the laser scan direction.

2.4. MTF and Resolution Quantification

The discrimination of structures 60 µm apart in Figure 3c,d already provides a >4-time gain over the theoretical diffraction-limited resolution of the employed thermal camera. Aiming at quantifying the actual SR capabilities of the proposed

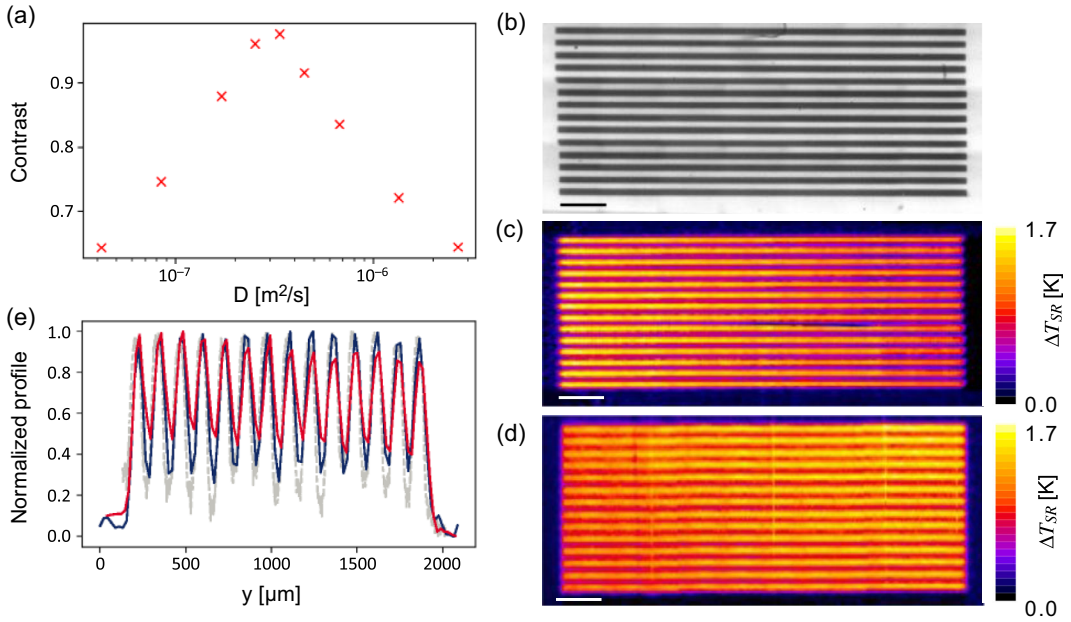

Figure 3. Proof-of-principle model-based SR image reconstruction: dependence on the sample thermal diffusivity and the scan path. a) Contrast of the SR thermal image of the microfiche sample in Figure 2a as a function of the thermal diffusivity assumed in the reconstruction algorithm. Images have been derived from the same dataset of Figure 2c; the highest contrast is achieved for the correct value $D = 3.35 \times 10^{-7}\ m^2\ s^{-1}$ as imposed in Figure 2c (see Figure S4, Supporting Information). b) 633 nm transmitted-light image of the microfiche-printed striped pattern. c,d) SR thermal images of the microfiche sample in (b) acquired by laser raster scanning with parameters $N_x \times N_y = 240 \times 120$, $\Delta x = 22.2$µm, $\tau_{on} = 50$ms, $\omega = 28$µm; the scan is parallel and orthogonal to the ink lines in (c,d), respectively. Scale bars: 500 µm in (b–d). e) Normalized intensity and temperature profiles extracted along the vertical direction in (b–d) (gray, blue, and red, respectively). All datasets have been acquired with the camera FLIR T650sc.

approach and at demonstrating the possibility of performing SR thermography down to the microscale, the MTF and PSF of the imaging system have been experimentally characterized by the so-called knife-edge method.[28] The excitation laser beam has been focused at first to a 7 μm waist and SR thermal images have been acquired for varying scan pixel size and pixel dwell time across the interface of black matte tape on a glass coverslip (Methods section and **Figure 4**a). An optical transmitted-light image of the sample has been acquired as reference ground-truth frame and the normalized intensity profile, extracted orthogonally to the tape interface, has been superimposed to the corresponding profile (the edge spread function, ESF) from the reconstructed SR thermal images.

Provided the laser waist is oversampled with 3 μm scan pixel size Δx, the reconstructed thermal image and ESF are only slightly affected by the pixel dwell time in the 10–100 ms range (Figure 4a). At fixed 100 ms dwell time, larger scan pixel sizes broaden instead the reconstructed ESF, as expected (Figure 4b). The best recovered PSF, obtained as the first derivative of the ESF for 100 ms dwell time and 3 μm scan pixel size, is reported in Figure 4c and provides a full width at half maximum (FWHM) and an achievable resolution of 29 ± 1 μm. The MTF correspondingly reaches a 10% threshold amplitude at about 0.03 line pairs/μm (Figure 4d).

Higher spatial resolution can be finally achieved by further focusing the excitation beam to a submicron waist. Indeed, a thermal ESF that perfectly overlaps with the transmitted-light intensity profile is reconstructed at 0.9 μm laser waist and 2 μm scan pixel size with a pixel dwell time as low as 30 ms (Figure 4e). The (5.6 ± 0.5) μm width of the derived PSF, which corresponds to a MTF decaying at 0.3 line pairs/μm (Figure S5, Supporting Information), confirms that the spatial resolution is now only limited by the sharpness of the imaged interface (Figure 4f). Such a 5.6 μm resolution demonstrates a ≈200-time gain over the millimeter-sized thermally diffused point spread function (Figure S1, Supporting Information) of the camera in its conventional operation on the seconds timescale.

2.5. Microscale SR Photothermal Imaging on Biological Tissues

The achievement of ≲5 μm spatial resolution, quantified by PSF and MTF measurements in Figure 4, has been finally exploited in

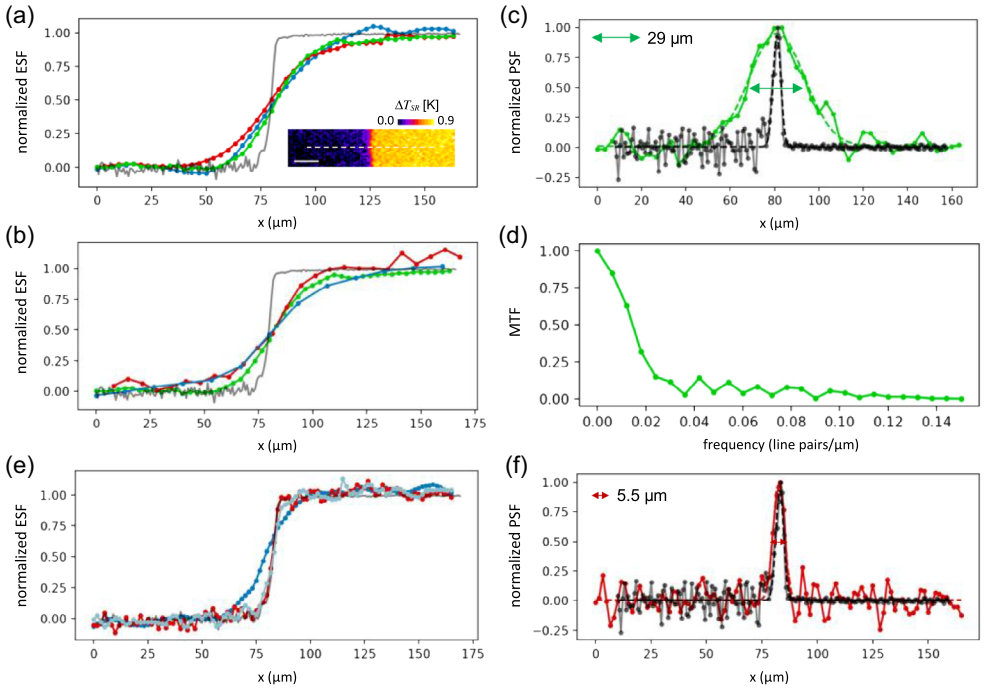

Figure 4. PSF and MTF measurements. (a, inset) Exemplary SR thermal image of the edge of black photothermal tape on a 170 μm thick glass coverslip; scale bar: 20 μm. a) Normalized profiles (ESFs) extracted from the optical transmitted-light image of the sample (gray line) and from the reconstructed SR thermal images (colored circles) in the direction orthogonal to the tape edge with $\omega = 7$ μm, $\Delta x = 3.3$ μm; colors identify the dwell time τ_{on} (10 ms, blue; 50 ms, red; 100 ms, green). b) Same as (a), with colors coding for the scan pixel size Δx (3.3 μm, green; 6.6 μm, red; 13.3 μm, blue) at fixed $\tau_{on} = 100$ ms and $\omega = 7$ μm. c) Gray: first derivative of the transmitted-light ESF in (a); note that variable noise levels across the PSF profile are due to the different noise levels in the two portions of the corresponding ESF profile that lie outside and inside the imaged black tape. Data are overlaid to the best Gaussian fit (dashed line). Green: normalized PSF computed as the first derivative of the thermal ESF reported for $\tau_{on} = 100$ ms in (a), overlaid to the best Gaussian fit (dashed line); the (29 ± 1) μm Gaussian FWHM defines the achievable spatial resolution of the SR imaging system at 7 μm laser waist. d) MTF computed as the magnitude of the fast Fourier transform of the thermal PSF in (c). e) Normalized ESFs extracted from the optical transmitted-light image of the sample (gray line) and from the reconstructed SR thermal images (colored circles) orthogonally to the tape edge; colors identify τ_{on} (10 ms, blue; 30 ms, light blue; 50 ms, red); $\omega = 0.9$ μm, $\Delta x = 1.7$ μm. f) Gray: first derivative of the transmitted-light ESF in panel (e), overlaid to the best Gaussian fit (dashed grey line). Red: normalized PSF computed as the first derivative of the thermal ESF reported for $\tau_{on} = 50$ ms in (e), overlaid to the best Gaussian fit (dashed red line). All the thermal images have been collected on the FLIR E40 camera.

an exemplary application of high-resolution model-based thermal image reconstruction on biological tissues ex vivo. To this aim, human liver needle biopsies extracted from patients diagnosed with HH[29,30] and subjected to the modified Perls' PB iron staining[31] have been employed.

HH consists in the clinically most important systemic pathological condition associated with iron accumulation in the liver.[29] Even though such an inherited disorder of iron metabolism is efficiently identified by genetic testing, imaging-based liver analysis is required to grade hepatic iron deposition histologically[29]: grade increases for increasing amounts of iron and for the progressive involvement of hepatocytes from the periportal to the pericentral areas,[29,30] so that the quantification of iron depositions and the visual inspection of their spatial distribution in liver biopsy specimens is important for assessing the stage and severity of hepatic iron overload.

By the Perls' PB iron staining, insoluble PB pigments form in the tissue when deposited ferric iron reacts with the potassium ferrocyanide in the stain. PB exhibits highly efficient thermal relaxation upon absorption of visible/near-IR laser light, thereby suggesting the possibility of successfully visualizing and mapping iron by SR photoactivated thermography. At the same time, PB pigments appear as blue to purple deposits in RGB optical images of the tissue collected under white-light widefield illumination: given the availability of such a reference ground truth image, PB-stained liver biopsies appear as ideal candidates to validate the spatial resolution claimed for SR model-based thermal imaging on biological samples.

Results are shown in **Figure 5**. A ROI of the RGB optical image of a modified Perls' PB-stained human liver biopsy (Figure 5a) is compared with the corresponding super-resolved thermal image (Figure 5b) acquired by sample raster scanning at 800 nm laser excitation. Colocalization is observed between the temperature variations in the SR image and the PB deposits in the wide-field optical image, thereby confirming the specificity of the detected thermal signal. The possibility of imaging PB at microscale resolution is demonstrated by details as close as 4 µm being resolved in Figure 5b: such a high gain over the resolution of conventional thermography appears particularly evident when noting that the entire field of view of Figure 5 is contained within a single thermal camera pixel on the sample plane.

The analysis reported here for a single excitation wavelength can be easily expanded to a multiwavelength approach and to a spectral analysis of the photothermal signal. In this way, one could identify different absorbers in the tissue. It is also finally worth remarking that Figure 5b has been acquired and reconstructed by combining a low-cost (≈5 k€) commercial thermal camera with an optical laser scanning microscope. Whether based on laser scanning by galvanometric mirrors or on sample scanning via piezostages, raster-scanned illumination is always available on commercial confocal and multiphoton excitation microscopes: therefore, the implementation of model-based SR thermography practically only requires the addition of a thermal camera in transmission geometry to the existing experimental setup, and SR photothermal imaging could be combined with optical (fluorescence) contrast in a multimodal imaging approach with no substantial hardware modification. As chromophores with high fluorescence quantum yields are typically inefficient

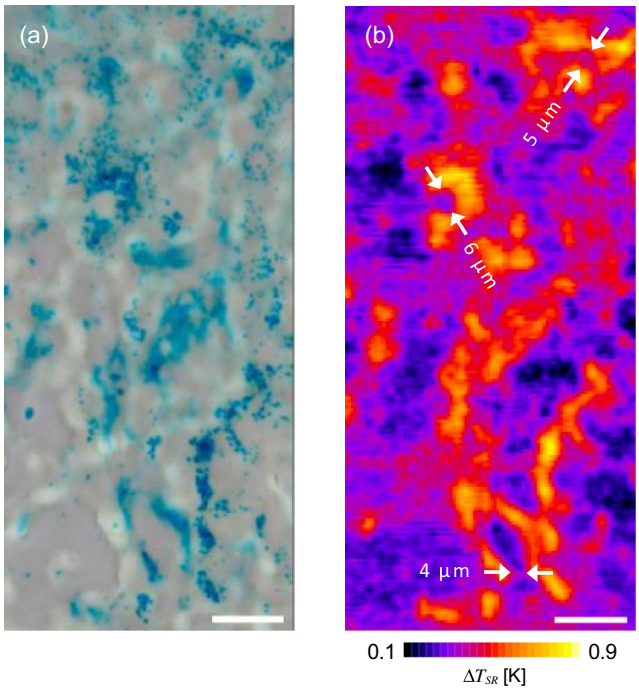

Figure 5. SR photothermal imaging on human liver tissue ex vivo. a) RGB image of a ROI of a human liver biopsy stained by the modified Perl's PB method. b) SR thermal image of the sample in (a), acquired by laser raster scanning with parameters $\Delta x = 0.8\,\mu m$ and $\tau_{on} = 100\,ms$ and reconstructed by Equation (9). The image has been assembled as a mosaic of eight tiles, each tile having format $N_x \times N_y = 62 \times 62$, and has been filtered with the built-in smoothing plugin in FiJi software; the raw (unsmoothed) reconstructed SR image is reported in Figure S6, Supporting Information. Scale bars: 20 µm. Datasets have been acquired with the camera FLIR E40.

in thermal relaxation and vice versa, SR thermography and fluorescence imaging are expected to provide complementary information when applied (simultaneously) on the very same specimens and fields of view.

3. Conclusion

SR approaches have revolutionized the quantitative inspection of biological samples by optical imaging. The development of SR far-field optical microscopy techniques, capable of pushing the resolution limit to length scales of only a fraction of the visible imaging wavelength, has indeed shed new light onto details of the cellular architecture that were previously inaccessible by conventional diffraction-limited imaging.[7,32] On a similar note, SR methods can be exploited to enhance and broaden the applicability of imaging modalities operating beyond the visible spectral range. In this work, we take advantage of a commercial low-cost camera operating in the far-IR and exploit SR model-based reconstruction to push the resolution of photoactivated thermal imaging down to the microscale. By incorporating both thermal diffusion effects and diffraction-limited signal detection in a full-wave forward model of the imaging system, and by iteratively solving the corresponding inverse problem, we provide the

super-resolved localization of the photothermal entities at the sample surface while preserving the quantification of the laser-induced temperature profile. The experimental point spread function quantified by the knife-edge method in Figure 4 and the results of tissue imaging in Figure 5 have demonstrated the achievement of <5 μm radial spatial resolution. Such a result, that has been obtained with an inexpensive camera with 0.1 K sensitivity and noise equivalent temperature difference, is expected to further improve with the use of higher quality cameras in terms of both data signal-to-noise ratio and required minimum excitation laser powers.

The demonstrated resolution enhancement of model-based imaging is combined here with minute-long data acquisition, with a 60-fold reduction in the acquisition time shown in Figure 2 with respect to our previously developed SR strategy based on the localization of sparsely primed temperature variations.[9] Model- and localization-based[9] SR strategies appear overall as complementary techniques: model-based reconstruction provides the advantage of higher spatial resolutions and shorter imaging time at the price of a required prior knowledge of the sample thermal properties; localization-based (model-free) imaging requires up-to-hour-long data acquisition instead, but does not assume any sample property, to the point that thermal conductivity values can be extracted and spatially mapped from SR temperature-based images.[24] The accommodation of spatially heterogenous thermal conductivity/diffusivity values in model-based image inversion is the object of our currently ongoing work, aimed at providing model-based thermography with the possibility of discriminating elemental/phase features on inhomogeneous and composite specimens.

Chemical specificity in IR imaging is currently enabled by the recently developed O-PTIR (optical photothermal infrared) technique, which takes advantage of a tunable modulated IR laser (e.g., a quantum cascade laser in the fingerprint wavenumber region at 1800–800 cm^{-1}) to prime the sample photothermal expansion: by monitoring the change in the elastically (Rayleigh) scattered light of a visible-wavelength probe laser beam, O-PTIR allows the acquisition of vibrational spectra analogous to those provided by traditional Fourier transform infrared, at the submicrometer spatial resolution imposed by diffraction of the employed visible wavelength probe beam.[33–35] Reaching applicability to heterogenous samples, which is in our opinion the major advantage of O-PTIR over SR IR thermography, is foreseen as the natural upcoming development of the proposed thermal imaging approach.

The exploitation of a full-wave forward model of image formation and the reconstruction of super-resolved information by the solution of the inverse problem is shared by SR methods in a variety of imaging modalities, ranging from confocal fluorescence microscopy in the visible spectral range[36] to mid-IR thermography. Such SR thermographic techniques have been targeted to the 3D identification and reconstruction of subsurface material defects in nondestructive testing on the millimeter spatial scale,[21] whereas model-based reconstruction is specifically directed here to the enhancement of the radial spatial resolution. Provided that photothermal entities can now be investigated at <5 μm—i.e., single cell level—spatial resolution, our results expand the applicability of photoactivated thermography in the life sciences and in the investigation of biological samples well below the tissue spatial scale. Applications have been suggested in the literature for the investigation of microscale thermal phenomena in phase transitions and for the characterization of the latent heat of freezing for cells in cryopreservation, as demonstrated with IR cameras coupled with achromatic microlens optics.[37,38] We further envision promising applications in the label-free characterization of endogenous photothermal biomarkers (e.g., hemoglobin, melanin pigments) in biological tissue sections, and foresee that model-based image reconstruction will strengthen and expand the results we have previously obtained in the quantification of the melanin content in murine melanoma biopsies.[22,23]

Concerning the technique applicability, it is finally worth remarking that model-based SR thermal imaging is not associated, in principle, to any requirement in terms of sample far-IR emissivity: assumed that the sample has photothermal properties and that the excitation laser wavelength lies within the absorption band of the sample itself, comparable signal-to-noise ratios could be experimentally achieved on samples with different far-IR emissivity by the only adjustment of the excitation laser power. Still, plenty of materials of practical interest display high emissivity, with ε values at 300 K being typically higher than 0.8 and 0.6 for nonmetals[39] and oxidized metals,[25] respectively. Practical limitations could involve metals in highly polished state ($\varepsilon < 0.1$[25]): these materials, which are generally highly reflective in the visible spectrum too, do not display prominent one-photon absorption upon focused low-power visible laser-light illumination, thereby preventing application of the proposed imaging strategy irrespective of the exact emissivity value. We conclude that the presence of heat release upon focused laser-light absorption remains the only major prerequisite for SR far-IR thermography.

Supporting Information

Supporting Information is available from the Wiley Online Library or from the author.

Acknowledgements

M.M. and L.P. contributed equally to this work. The authors are grateful to Prof. Roberto Colombo (Department of Earth and Environmental Sciences, Università degli Studi di Milano-Bicocca, 20126, Milano, Italy) for kindly lending the FLIR T650sc thermal camera. The authors acknowledge funding from Università degli Studi di Milano-Bicocca (grant no. 2020-ATESP-0008 to G.C.).

Conflict of Interest

The authors declare no conflict of interest.

Data Availability Statement

The data that support the findings of this study are available from the corresponding author upon reasonable request.

Keywords

infrared imaging, model-based image reconstruction, photothermal effect, super-resolution imaging methods, thermography

Received: August 25, 2023
Revised: October 5, 2023
Published online: November 8, 2023

[1] M. Vollmer, K. P. Möllmann, *Infrared Thermal Imaging: Fundamentals, Research and Applications*, Wiley-VCH, Weinheim, Germany **2017**.
[2] R. Usamentiaga, P. Venegas, J. Guerediaga, L. Vega, J. Molleda, F. G. Bulnes, *Sensors* **2014**, *14*, 12305.
[3] A. Rogalski, in *Proc. SPIE 10433, Electro-Optical and Infrared Systems: Technology and Applications XIV*, SPIE Security + Defence, Warsaw, Poland, September 11–14, **2017**, p. 104330L, https://doi.org/10.1117/12.2300779.
[4] K. Tang, K. Dong, C. J. Nicolai, Y. Li, J. Li, S. Lou, C.-W. Qiu, D. H. Raulet, J. Yao, J. Wu, *Sci. Adv.* **2020**, *6*, https://doi.org/10.1126/sciadv.abd8688.
[5] P. Burgholzer, T. Berer, J. Gruber, G. Mayr, *Appl. Phys. Lett.* **2017**, *111*, 031908.
[6] E. Abbe, *Archiv für Mikroskopische Anatomie* **1873**, *9*, 413.
[7] S. W. Hell, *Nat. Methods* **2009**, *6*, 24.
[8] P. Burgholzer, T. Berer, M. Ziegler, E. Thiel, S. Ahmadi, J. Gruber, G. Mayr, G. Hendorfer, *Quant. Infrared Thermogr. J.* **2020**, *17*, 268.
[9] M. Bouzin, M. Marini, A. Zeynali, M. Borzenkov, L. Sironi, L. D'Alfonso, F. Mingozzi, F. Granucci, P. Pallavicini, G. Chirico, M. Collini, *Nat. Commun.* **2019**, *10*, 5523.
[10] S. Ahmadi, P. Burgholzer, G. Mayr, P. Jung, G. Caire, M. Ziegler, *NDT and E Int.* **2020**, *111*, 102228.
[11] S. Ahmadi, G. Thummerer, S. Breitwieser, G. Mayr, J. Lecompagnon, P. Burgholzer, P. Jung, G. Caire, M. Ziegler, *IEEE Trans. Ind. Inf.* **2021**, *17*, 7368.
[12] S. Ahmadi, J. Lecompagnon, P. D. Hirsch, P. Burgholzer, P. Jung, G. Caire, M. Ziegler, *Sci. Rep.* **2020**, *10*, 22357.
[13] E. Mandanici, L. Tavasci, F. Corsini, S. Gandolfi, *Appl. Geomatics* **2019**, *11*, 215.
[14] M. S. Alam, J. G. Bognar, R. C. Hardie, B. J. Yasuda, *IEEE Trans. Instrum. Meas.* **2000**, *49*, 915.
[15] L. Cheng, M. Kersemans, *Compos. B Eng.* **2022**, *247*, 110309.
[16] H. Gupta, K. Mitra, *IEEE Trans. Image Process.* **2022**, *31*, 433.
[17] C. Dong, C. C. Loy, K. He, X. Tang, *IEEE Trans. Pattern Anal. Mach. Intell.* **2016**, *38*, 295.
[18] R. E. Rivadeneira, A. D. Sappa, B. X. Vintimilla, in *VISIGRAPP 2020 – Proc. of the 15th Int. Joint Conf. on Computer Vision, Imaging and Computer Graphics Theory and Applications*, SciTePress, Valletta, Malta, February 27–29, **2020**, pp. 111–119.
[19] Y. He, B. Deng, H. Wang, L. Cheng, K. Zhou, S. Cai, F. Ciampa, *Infrared Phys. Technol.* **2021**, *116*, 103754.
[20] S. Ahmadi, P. Burgholzer, P. Jung, G. Caire, M. Ziegler, *Opt. Lasers Eng.* **2020**, *134*, 106279.
[21] J. Lecompagnon, S. Ahmadi, P. Hirsch, C. Rupprecht, M. Ziegler, *J. Appl. Phys.* **2022**, *131*, 185107.
[22] M. Bouzin, M. Marini, G. Chirico, F. Granucci, F. Mingozzi, R. Colombo, L. D. Alfonso, L. Sironi, M. Collini, *Biomed. Opt. Express* **2022**, *13*, 1173.
[23] M. Marini, M. Bouzin, R. Scodellaro, L. D'Alfonso, L. Sironi, F. Granucci, F. Mingozzi, G. Chirico, M. Collini, *Biomol. Concepts* **2022**, *13*, 242.
[24] M. Marini, M. Bouzin, L. Sironi, L. D'Alfonso, R. Colombo, D. Di Martino, G. Gorini, M. Collini, G. Chirico, *Mater. Today Phys.* **2021**, *18*, 100375.
[25] D. Bäuerle, *Laser Processing and Chemistry*, Springer-Verlag Berlin, Heidelberg, Germany **2011**.
[26] M. Marini, A. Zeynali, M. Collini, M. Bouzin, L. Sironi, L. D'Alfonso, F. Mantegazza, V. Cassina, G. Chirico, *Lab Chip* **2022**, *22*, 4917.
[27] H. Ogi, T. Ishihara, H. Ishida, A. Nagakubo, N. Nakamura, M. Hirao, *Phys. Rev. Lett.* **2016**, *117*, 195901.
[28] H. Zhang, C. Li, Y. Duan, *Optik (Stuttg)* **2018**, *157*, 635.
[29] K. P. Batts, *Mod. Pathol.* **2007**, *20*, 31.
[30] N. Subramaniam, *World J. Gastroenterol.* **2007**, *13*, 4755.
[31] J. H. Lefkowitch, *Semin. Diagn. Pathol* **2006**, *23*, 190.
[32] E. Betzig, G. H. Patterson, R. Sougrat, O. W. Lindwasser, S. Olenych, J. S. Bonifacino, M. W. Davidson, J. Lippincott-Schwartz, H. F. Hess, *Science* **2006**, *313*, 1642.
[33] D. Zhang, C. Li, C. Zhang, M. N. Slipchenko, G. Eakins, J. X. Cheng, *Sci. Adv.* **2016**, *2*, https://doi.org/10.1126/sciadv.1600521.
[34] C. Marcott, M. Kansiz, E. Dillon, D. Cook, M. N. Mang, I. Noda, *J. Mol. Struct.* **2020**, *1210*, 128045.
[35] A. Marchetti, V. Beltran, G. Nuyts, F. Borondics, S. De Meyer, M. Van Bos, J. Jaroszewicz, E. Otten, M. Debulpaep, K. De Wael, *Sci. Adv.* **2022**, *8*, https://doi.org/10.1126/sciadv.abl6769.
[36] R. Chen, M. Wu, J. Ling, Z. Wei, Z. Chen, M. Hong, X. Chen, *Optica* **2016**, *3*, 1339.
[37] J. Morikawa, E. Hayakawa, T. Hashimoto, in *Proc. SPIE 8354, Thermosense: Thermal Infrared Applications XXXIV*, SPIE Defense, Security, and Sensing, Baltimore, Maryland, United States, April 23–27, **2012**, p. 835410, https://doi.org/10.1117/12.918252.
[38] C. Pradere, M. Junko, J. Toutain, J. C. Batsale, E. Hayakawa, T. Hashimoto, *Quant. Infrared Thermogr. J.* **2009**, *6*, 37.
[39] M. Quinn Brewster, *Thermal Radiative Transfer and Properties*, John Wiley & Sons, Hoboken, NJ, USA **1992**.